Supporting Information for

Microstructured Ceramic-Coated Carbon Nanotube Surfaces for High Heat Flux Pool Boiling

Hangbo Zhao[†], Susmita Dash[†‡], Navdeep Singh Dhillon[†], Sanha Kim[†], Bethany Lettiere[†], Kripa K. Varanasi[†], and A. John Hart[†,*]

[†]*Department of Mechanical Engineering and Laboratory for Manufacturing and Productivity, Massachusetts Institute of Technology, 77 Massachusetts Avenue, Cambridge, Massachusetts, 02139, USA.*

[‡] *Department of Mechanical Engineering, Indian Institute of Science, Bangalore, 560012, India.*

* Corresponding author: ajhart@mit.edu

List of Contents

Captions for Videos S1-S2:

Video S1. Synchronized high-speed optical and infrared video (slowed down 100X) showing boiling on an Al_2O_3-CNT micropillar array with 15 nm Al_2O_3 coating thickness, at a heat flux q" = 30 W·cm^{-2}.

Video S2. Synchronized high-speed optical and infrared video (slowed down 100X) showing boiling on an Al_2O_3-CNT micropillar array with 15 nm Al_2O_3 coating thickness, at a heat flux q" = 230 W·cm^{-2}.

Temperature measurement from infrared imaging

A temperature calibration is used to relate the infrared counts from infrared imaging to the absolute temperature of the infrared-opaque Ti heater (150 nm) on the back of the substrate (see Figure S1). Details of the calibration procedure can be found in an earlier work.[1] The use of the Ti heater ensures that the difference in the infrared count is solely due to the difference in the temperature of the Ti layer. The surface temperature on the Al_2O_3 surface (i.e. between CNT micropillars) is calculated using Fourier's law by calculating the temperature difference between the backside Ti and the top Al_2O_3 surface:

$$T_s = T_b - q'' \cdot \left(\frac{t_{Si}}{k_{Si}} + \frac{t_{SiO_2}}{k_{SiO_2}} + \frac{t_{Al_2O_3}}{k_{Al_2O_3}}\right) \quad (1)$$

where T_s and T_b are the temperatures at the top Al_2O_3 surface and the back Ti heater, respectively; q'' is the applied heat flux, t_{Si}/k_{Si}, t_{SiO_2}/k_{SiO_2}, and $t_{Al_2O_3}/k_{Al_2O_3}$ are the thickness/thermal conductivity of the Si, SiO_2, and Al_2O_3 layer, respectively. The corresponding values (at 100°C) are listed below:

	Si	SiO_2	Al_2O_3
Thickness (μm)	650	300 + 300	0.015 (15 nm) or 0.05 (50 nm)
Thermal conductivity ($W \cdot m^{-1} \cdot K^{-1}$)	110	1.3 (thermally grown)	2 (deposited by ALD[2])

The calculated temperature at the top, flat Al_2O_3 surface is then taken as the wall temperature for the plot of the boiling curves.

Uncertainty of measurements

The uncertainty of heat flux measurement is minimal since it is set and controlled by a LabVIEW program to maintain constant set power values. For the wall temperature measurement, the uncertainty mainly originates from the additional thermal resistance of CNT-covered region because the temperature of the top, flat Al_2O_3 surface is taken to be the wall temperature without taking into account the thermal resistance of the CNT layer during boiling.

The effective bulk thermal conductivity of vertically aligned CNTs with 10-14 μm thickness and 15 nm Al_2O_3 coating in ambient air is reported to be approximately 3.8 $W \cdot m^{-1} \cdot K^{-1}$.[3] Without considering the liquid imbibition into the porous Al_2O_3-coated CNT micropillars, the temperature difference between the top, flat Al_2O_3 surface (bottom surface of the Al_2O_3-CNT micropillars) and the top surface of the Al_2O_3-

CNT micropillars at the maximum heat flux (245 W·cm^{-2}) is calculated to be ΔT ~6.4°C. And this temperature difference scales linearly with the applied heat flux. This indicates that the temperature at the top surface of the Al_2O_3-CNT micropillars during boiling is lower than that of the measured temperature with an upper bound of 6.4°C. Considering the imbibed water during boiling has a much higher thermal conductivity (~680 mW·m^{-1}·K^{-1} at 100°C) than that of air (~26 mW·m^{-1}·K^{-1}), the actual temperature difference across the Al_2O_3-CNT micropillars during boiling is smaller than 6.4°C, even at the maximum heat flux measured. For CNT micropillars with 50 nm Al_2O_3 coating, the temperature difference across the CNT layer is even smaller given the larger volume fraction of Al_2O_3-CNTs. Moreover, the area fraction of CNT coverage on the total boiling surface is $\pi a^2 / p^2$~0.5. Therefore, the temperature measured and calculated at the top Al_2O_3 surface from infrared imaging can reasonably represent the boiling wall temperature.

It is worth noting that for much taller CNT structures, the bulk thermal resistance across the CNT layer can be much larger due to the density decay of CNT forests as the height increases.[4] This explains the large thermal resistance and corresponding temperature drop observed in our experiments across the tall (130 μm and 50 μm) Al_2O_3-CNT microstructures.

Analysis of liquid imbibition

On the microstructured CNT surfaces, imbibition occurs at the microtexture level (i.e., between the CNT pillars), and at the nanoscale level within the Al_2O_3-coated CNTs.

Microscale imbibition (between pillars)

The microscale imbibition on Al_2O_3-coated CNT microstructures is illustrated in Figure 5a (left). The liquid imbibition process is driven by the capillary force F_c, which is balanced by the viscous drag from the substrate F_1 and the sidewalls of the micropillars F_2. The capillary driving force can be derived using a work-energy method. First, consider a unit cell in the square array of micropillars, as indicated by the red dotted box in Figure 5a with a dimension of $p \times p$. The surface energy change of liquid wetting this unit cell (ignore wetting of the top surface of the pillars) can be decomposed into the following 3 parts:

The loss of the solid-vapor surface energy is

$$\Delta E_1 = -[p^2 - \pi a^2 + r \cdot 2\pi a h] \cdot \sigma_{SV} \quad (2)$$

where r is the surface roughness of the micropillar sidewalls.

The increase of the solid-liquid surface energy is

$$\Delta E_2 = [p^2 - \pi a^2 + r \cdot 2\pi a h] \cdot \sigma_{SL} \quad (3)$$

And the increase of the liquid-vapor surface energy is

$$\Delta E_3 = (p^2 - \pi a^2) \cdot \sigma_{LV} \tag{4}$$

Combining the above expressions, the total surface energy change of wetting a unit cell is

$$\begin{aligned} \Delta E &= \Delta E_1 + \Delta E_2 + \Delta E_3 \\ &= -(p^2 - \pi a^2 + r \cdot 2\pi a h)\sigma_{LV} \cos\theta + (p^2 - \pi a^2)\sigma_{LV} \end{aligned} \tag{5}$$

Here the Laplace equation is used

$$\sigma_{SV} - \sigma_{SL} = \sigma_{LV} \cos\theta \tag{6}$$

For nanoporous microstructures, the contact angle at the sidewalls reduces to zero due to nanoscale imbibition into the pores inside the micropillars. Here it is assumed that the nanoscale imbibition does not affect the microscale imbibition, which will be analyzed later. Therefore the term $r \cdot \cos\theta$ is replaced by 1 on the sidewalls of the microstructures.

Equation (5) can therefore be rewritten as

$$\Delta E = [(p^2 - \pi a^2)(1 - \cos\theta) - 2\pi a h]\sigma_{LV} \tag{7}$$

The capillary driving force (per unit width of the liquid film) is then

$$F_c = -\frac{\Delta E}{p^2} = \frac{\sigma_{LV}}{p^2}[2\pi a h - (p^2 - \pi a^2)(1 - \cos\theta)] \tag{8}$$

Note here the imbibition occurs only when $F_c > 0$, hence there exists a critical surface contact angle that enables imbibition:

$$\theta_{crit} = \cos^{-1}\left(1 - \frac{2\pi a h}{p^2 - \pi a^2}\right) \tag{9}$$

The viscous drag at the microscale has two components: viscous drag from the substrate and from the micropillar sidewalls. Assuming the imbibing liquid front velocity is V and the imbibition distance is L_m, the viscous drag from the substrate (per unit width of the liquid film) is estimated as

$$F_1 \approx \frac{2\mu V}{h} L_m \cdot \frac{p^2 - \pi a^2}{p^2} \tag{10}$$

Here a parabolic velocity profile in the z direction is assumed due to the boundary conditions: (1) at the substrate surface ($z = 0$), $V = 0$ as no-slip boundary condition applies; (2) at the shear-free top liquid surface ($z = h$), $\frac{\partial V}{\partial z} = 0$. The velocity gradient at the substrate can then be estimated as twice the average velocity gradient as in a parabolic velocity profile.

The viscous drag from the sidewalls of the micropillars F_2 can be estimated by considering the viscous drag from the individual cylinder. Sangani and Acrivos solved the resisting force per unit length on a cylinder for a uniform incoming flow across a square array of cylinders.[5] The closed-form expression has two parts corresponding to sparse and dense pillar arrays:

$$\frac{f}{\mu V} = \begin{cases} \dfrac{4\pi}{\ln \varepsilon^{-1/2} - 0.738 + \varepsilon - 0.887\varepsilon^2 + 2.038\varepsilon^3} & 0 < \varepsilon < 0.3 \\ \dfrac{9\pi}{2\sqrt{2}}[1 - (\dfrac{\varepsilon}{\varepsilon_{\max}})^{\frac{1}{2}}]^{-5/2} & 0.3 < \varepsilon < \varepsilon_{\max} \end{cases} \tag{11}$$

where ε is the solid volume fraction of the pillar arrays, which is

$$\varepsilon = \frac{\pi a^2}{p^2} \tag{12}$$

And $\varepsilon_{\max}$ is the solid volume fraction with the densest packing, which is

$$\varepsilon_{\max} = \frac{\pi}{4} \tag{13}$$

For simplicity, Equation (10) is rewritten as

$$\frac{f}{\mu V} \equiv C \tag{14}$$

The no-slip boundary condition at the substrate creates a velocity variation in the z direction, an average velocity $\overline{V}$ is used to estimate the viscous drag across the pillar height h. For a parabolic velocity profile,

$$\overline{V} \approx \frac{2}{3} V \tag{15}$$

Therefore the viscous drag from all the micropillars (per unit width of the liquid film) is

$$F_2 \approx \frac{2fh}{3}\frac{L}{p^2} = \frac{2\mu C}{3}\frac{hL_m}{p^2}V \tag{16}$$

A force balance between the capillary driving force and the viscous drag can be established

$$F_c = F_1 + F_2 \tag{17}$$

Substituting the expressions from Equation (8) into Equation (10) and Equation (16) gives

$$\sigma[2\pi ah - (p^2 - \pi a^2)(1 - \cos\theta)] = \mu V L_m[\frac{2(p^2 - \pi a^2)}{h} + \frac{2C}{3}h] \tag{18}$$

Substituting $V = \frac{dL_m}{dt}$ and integrating from $t = 0$ to $t = t$ gives the expression of the imbibition distance L_m:

$$L_m^{\,2} = \frac{2\sigma}{\mu} \cdot \frac{2\pi ah - (p^2 - \pi a^2)(1 - \cos\theta)}{\frac{2(p^2 - \pi a^2)}{h} + \frac{2C}{3}h} \cdot t \tag{19}$$

where the constant C is a function of the solid volume fraction as expressed in Equation (11). The microscale imbibition timescale for a distance of 2 mm (typical bubble radius at high heat flux) is $t_m \approx 0.2$ s. For micropillars with $a = 10$ μm, $h = 9$ μm, $\theta = 60^\circ$ (measured water contact angle on the flat Al_2O_3 area of the boiling sample prior to boiling experiment), with the pillar-pillar spacing $s = p - 2a$ be the variable, the imbibition time t can be calculated as a function of s and is plotted in Figure 5b. The blue curves correspond to expressions of Equation (11) for dense and sparse micropillar packing. The curves show that the micro-imbibition timescale has a minimum value at an intermediate micropillar spacing, which is $s_{opt} \approx 11$ μm. This is because of the tradeoff between capillary driving force and viscous drag: a too sparse pillar array does not provide a large capillary driving force, while for a too dense pillar array the viscous drag increases dramatically. The CNT micropillar samples in the boiling experiments have a spacing of $s = 5$ μm. To increase imbibition speed, the micropillar spacing could be changed to the optimum value s_{opt}.

Nanoscale imbibition (within the coated CNT forest)

In nanoscale imbibition, it is assumed that liquid is already imbibed into the micropillar array and therefore uniformly surrounds the pillar, and the imbibition direction is from the edge to the interior of the micropillar (Figure 5a, right). The Al_2O_3-coated CNTs within each micropillar are approximated as a square array of cylinders with diameter $2a_n$, pitch p_n and height h. Applying Darcy's law in the liquid imbibition direction x gives

$$\frac{Q}{A} = -\frac{k}{\mu}\frac{\partial p}{\partial x} \tag{20}$$

Applying the boundary conditions with the expression of the capillary pressure

$$P_c = \frac{2\sigma\cos\theta}{r_m} \tag{21}$$

The imbibition distance L_n can then be expressed as

$$L_n^{\,2} \approx \frac{4k\sigma\cos\theta}{\mu\phi r_m}\cdot t_n \tag{22}$$

where k is the permeability, ϕ is the porosity, and r_m is the pore radius. The nanoscale permeability k can be estimated based on a similar approximation of flow across a square array of nanoscale cylinders, which also have two regimes corresponding to sparse (thin Al_2O_3 coating) and dense (thick Al_2O_3 coating) arrays of Al_2O_3-CNTs. Their expressions can be found in a recent liquid imbibition study by Zhao *et al* [6]. From the SEM images, the diameter and spacing of the Al_2O_3-coated CNT forest can be estimated by taking multiple measurements. For the CNT micropillars with 150 ALD cycles (~ 15 nm) of Al_2O_3 coating, the average diameter and pitch are measured to be $2a_n \approx 36$ nm and $p_n \approx 78$ nm. Then the imbibition timescales can be calculated using Equation (22) and plotted as the orange curves in Figure 5b.

Analysis of boiling characteristics from infrared imaging

The IR video provides a two-dimensional picture of the infrared (IR) signal received through the backside of the sample, synchronized with the frames from the high-speed camera (Figure 3). These images show a clear bubble life-cycle, including bubble nucleation, growth, and departure from the heated surface. Further analysis of the bubble dynamics can be measured from the IR videos, following prior approaches[7]. Parameters of interests are the bubble nucleation cycle, growth time, wait time and the bubble departure diameter. Specifically, a vertical chord through the centerline of the IR images (Figure S7a, as indicated by the green arrow) gives a temporal stack of slices. In Figure S7, four bubble nucleation events are clearly recorded. After applying another chord cutting through the horizontal centerline, a grey value curve as a function of time is obtained based on the frame rate. The time between individual frames is 0.8 ms, given the frame rate of 1250 fps. The grey value curve in the plot in Figure S7c is directly related to the temperature at the center of the IR video frames, as indicated by the red dot in Figure S7a. From this plot, several features of the bubble cycle can be estimated, such as the bubble departure frequency, bubble growth time and bubble wait time (Figure S7c). The bubble cycle time t_c is the time between two adjacent bubble nucleation events. The bubble growth time t_g is the time between the beginning of bubble nucleation and the time the bubble reaches its maximum size (lowest grey value in a bubble cycle). The time between bubble departure and new bubble nucleation is the wait time t_w. Note that the bubble cycle time is the sum of the growth time and the wait time. Also, bubble departure diameter D is measured from the maximum size of the cold spot shown in Figure S7b.

References

1. Dash, S.; Rapoport, L.; Varanasi, K. K., Crystallization-Induced Fouling During Boiling: Formation Mechanisms to Mitigation Approaches. *Langmuir* **2018,** *34*, 782-788.
2. Cappella, A.; Battaglia, J.-L.; Schick, V.; Kusiak, A.; Lamperti, A.; Wiemer, C.; Hay, B., High Temperature Thermal Conductivity of Amorphous Al_2O_3 Thin Films Grown by Low Temperature ALD. *Adv. Eng. Mater.* **2013,** *15*, 1046-1050.
3. Vasquez, C. J. Oxide-Coated Vertically Aligned Carbon Nanotube Forests as Thermal Interface Materials. Georgia Institute of Technology, Ph.D. Thesis, **2014**.
4. Bedewy, M.; Meshot, E. R.; Reinker, M. J.; Hart, A. J., Population Growth Dynamics of Carbon Nanotubes. *ACS Nano* **2011,** *5*, 8974-8989.
5. Sangani, A. S.; Acrivos, A., Slow Flow Past Periodic Arrays of Cylinders with Application to Heat Transfer. *Int. J. Multiphase Flow* **1982,** *8*, 193-206.
6. Zhao, H.; Jacob, C.; Stone, H. A.; Hart, A. J., Liquid Imbibition in Ceramic-Coated Carbon Nanotube Films. *Langmuir* **2016,** *32*, 12686-12692.
7. Gerardi, C.; Buongiorno, J.; Hu, L.-W.; McKrell, T., Study of Bubble Growth in Water Pool Boiling through Synchronized, Infrared Thermometry and High-Speed Video. *Int. J. Heat Mass Transfer* **2010,** *53*, 4185-4192.

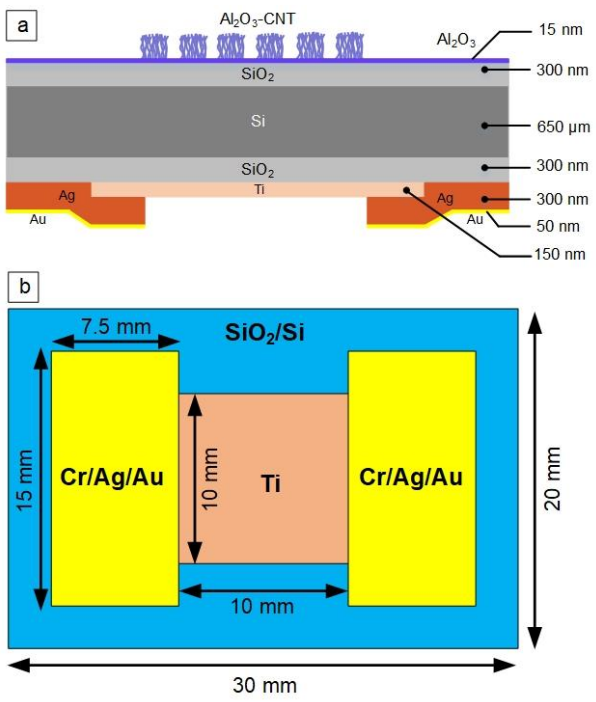

Figure S1. Sample configuration for pool boiling tests. (a) Schematic of the Al_2O_3-coated CNT microstructure sample configuration with heater and electrical contacts for pool boiling tests. (b) The configuration on the backside of the sample.

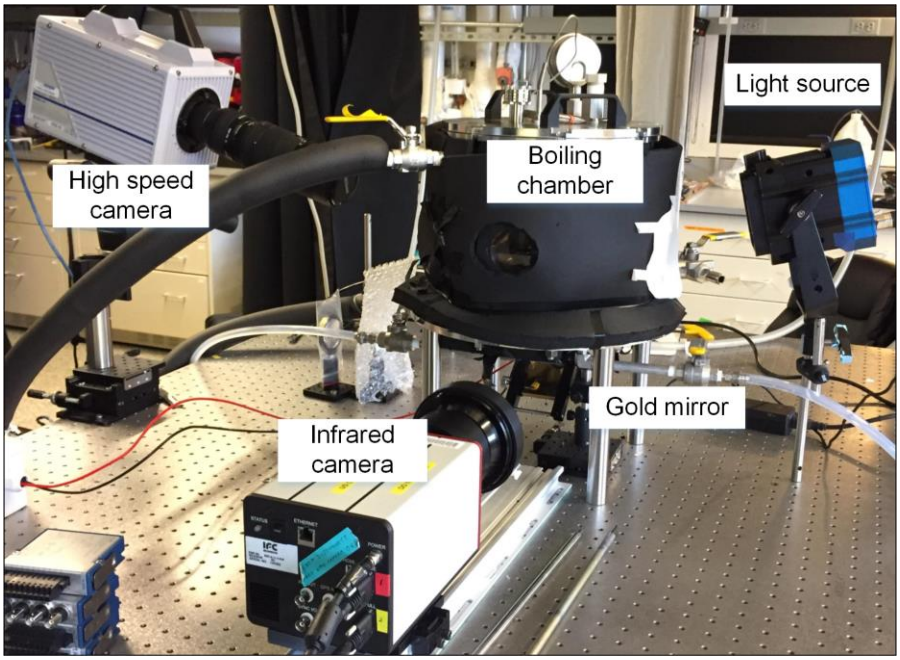

Figure S2. Photograph of the experimental setup for pool boiling experiments.

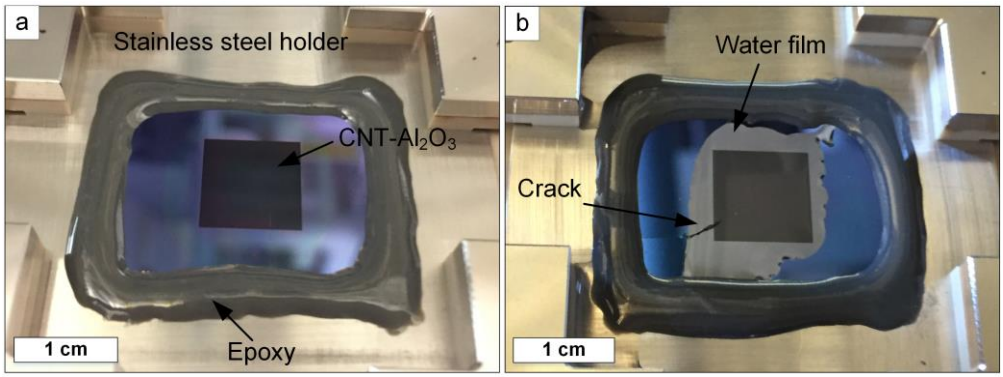

Figure S3. Photograph of the sample in the boiling chamber fixture (a) before and (b) after the boiling test. The sample fractured after CHF was reached due to the rapid temperature rise.

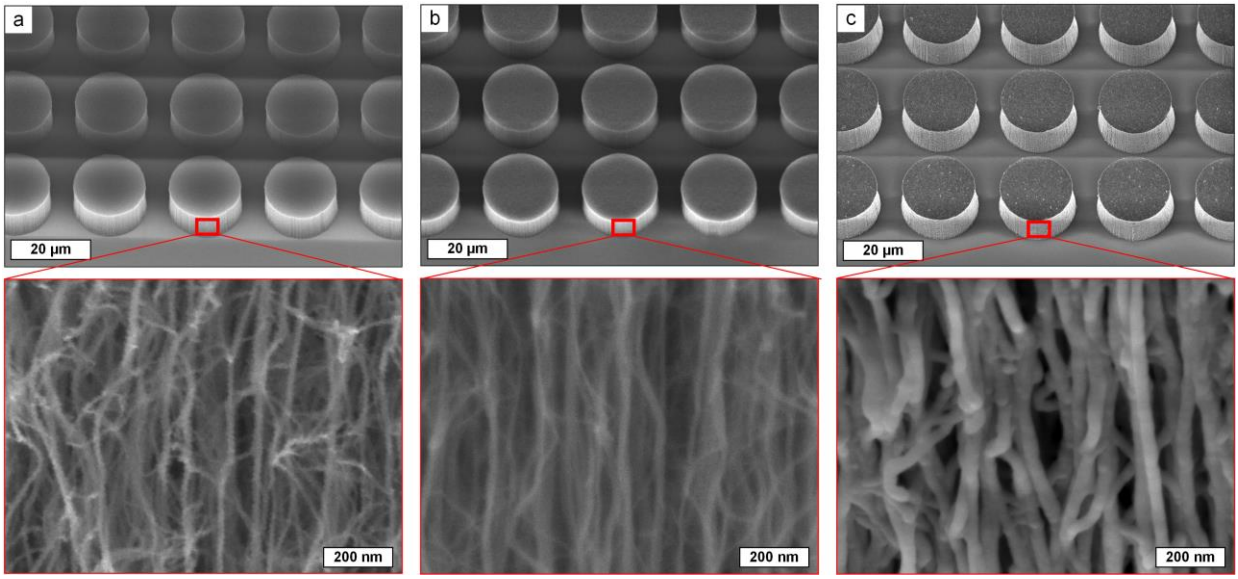

Figure S4. SEM images of CNT micropillars (a) before coating, and coated with (b) 2 nm (20 ALD cycles) and (c) 15 nm (150 ALD cycles) Al_2O_3 coating.

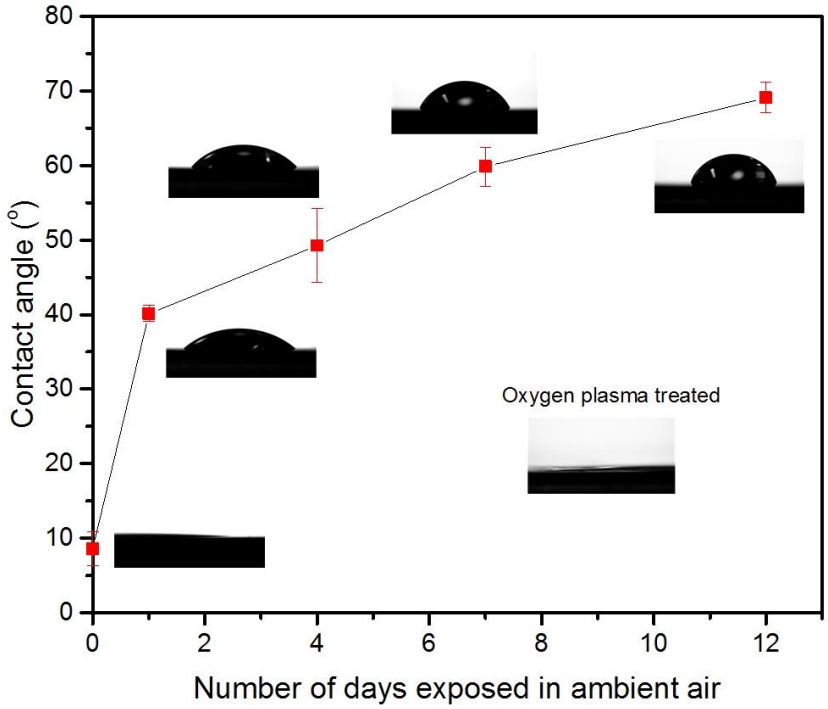

Figure S5. Water contact angles on a flat Al_2O_3 surface exposed in ambient air.

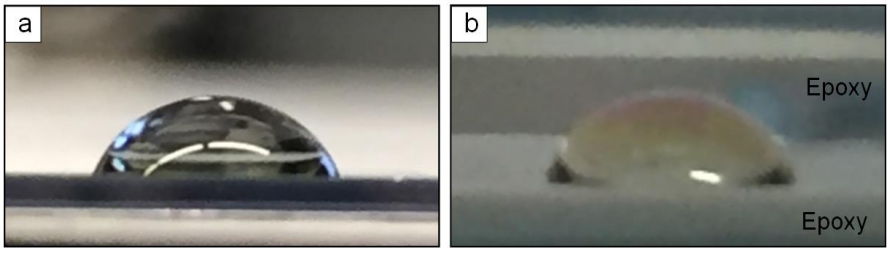

Figure S6. Photograph of a water drop on the flat Al_2O_3 surface (outside of the CNT-Al_2O_3 region) (a) before and (b) after the boiling test. The viewing angle in (b) was slightly tilted due to the existence of the surrounding epoxy layer.

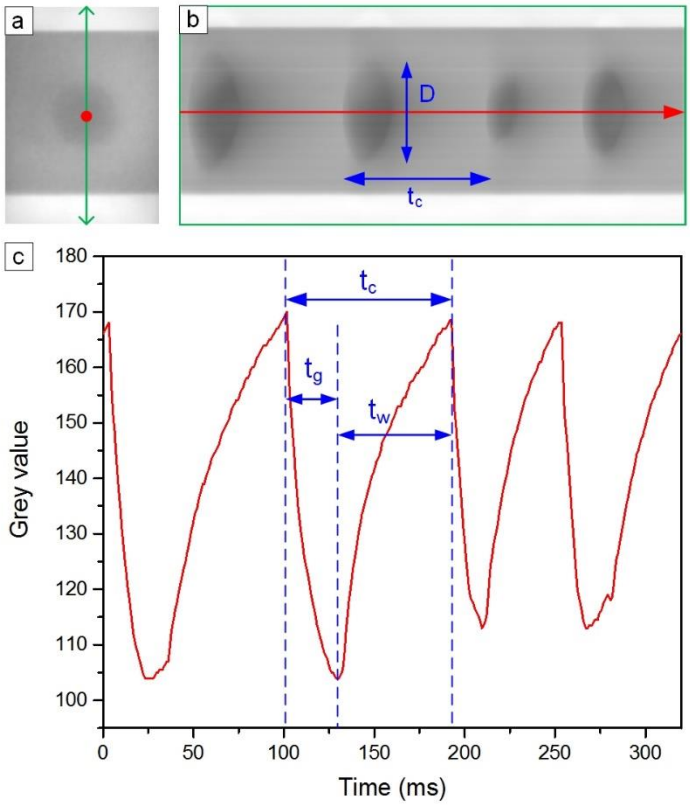

Figure S7. Measurement of timescales and bubble size from infrared imaging. (a) A frame of infrared video showing the bubble thermal footprint. (b) The temporal stack of slices from the centerline of the infrared video, as indicated by the green arrow in (a). (c) The time evolution of the grey value of the center point as indicated by the red dot in (a).

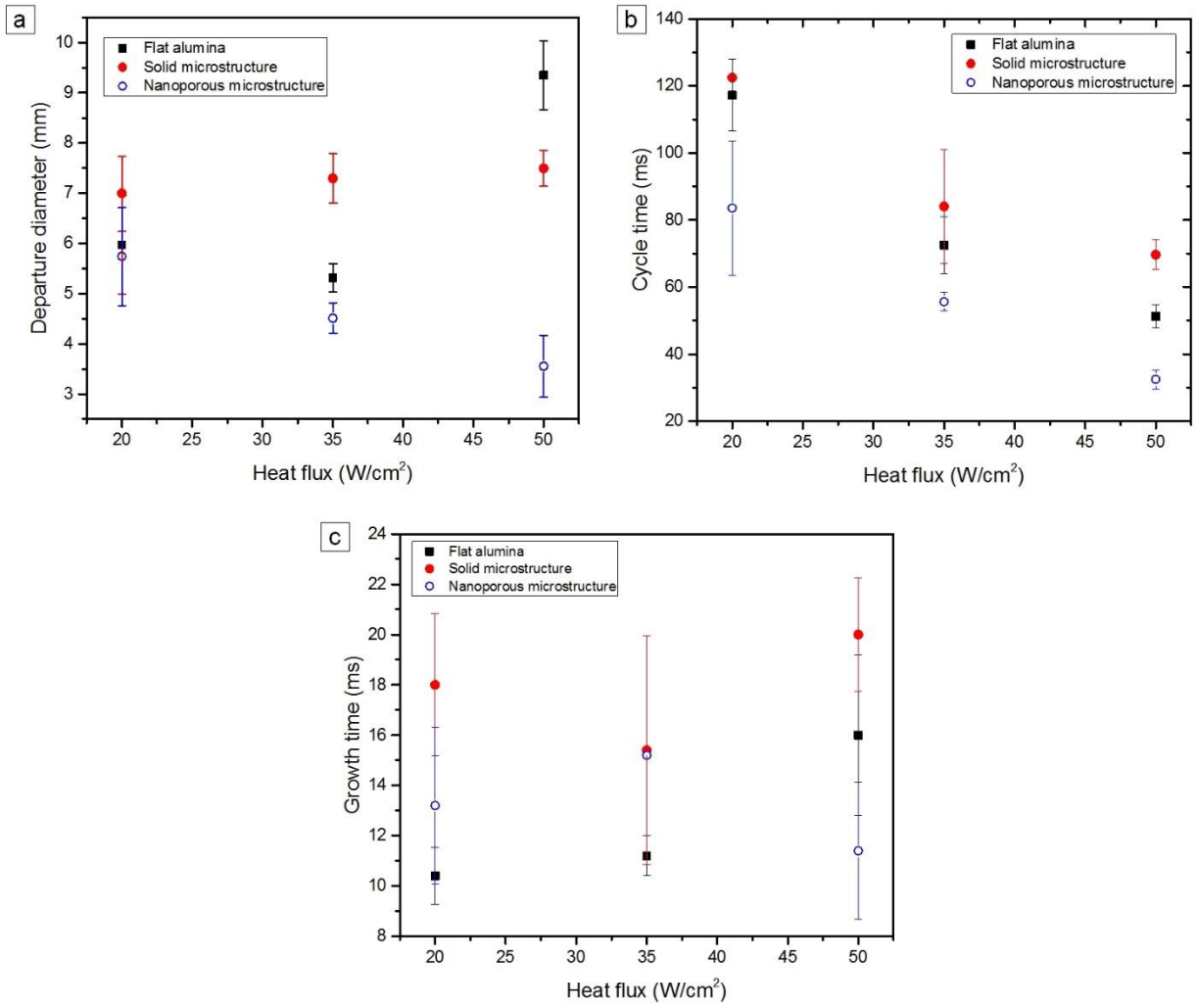

Figure S8. Comparison of the (a) bubble departure diameter, (b) bubble cycle time and (c) bubble growth time for boiling on a flat Al_2O_3 surface, solid Al_2O_3-CNT microstructures and nanoporous Al_2O_3-CNT microstructures at q" = 20 W·cm-2, 35 W·cm^{-2} and 50 W·cm^{-2}.